Simulation of gas turbine blade vibration measurement from unsteady casing wall pressure

Gareth L Forbes, Robert B Randall

School of Mechanical and Manufacturing Engineering, University of New South Wales, Sydney, NSW, 2052, Australia

ABSTRACT

Non-contact measurement of gas turbine blade vibrations has made significant progress over recent years; however, there still exist some limitations in the current techniques available. Specifically with blade tip timing (BTT) methods, some of the limitations are: the requirement of a large number of sensors for each engine stage, difficulties in dealing with multiple excitation frequencies, and sensors being located in the gas path. An alternative technique is examined here, utilising the unsteady casing wall pressure, which has the potential to rectify some of these limitations. Analytical simulation of the internal casing wall pressure is derived, for the situation with rotor blades undergoing forced vibration. The amplitude of the blade forced vibrations is then reconstructed from the simulated unsteady casing wall pressure, with results showing the robustness of the method to sensor location, measurement noise and a limited number of sensors.

INTRODUCTION

Gas turbine blade vibration measurement is motivated by the desire to acquire two principal pieces of information, either the blade's forced vibration magnitude and frequency, or to estimate the modal parameters of the blade. The impetus for this information is generally driven, respectively, by the need for knowledge of high cycle fatigue (HCF) estimates for blade life, or the use of blade modal parameter values for condition monitoring of the blades.

Measurement of blade vibration can be done directly with the attachment of strain gauges to the blade surface, however the attachment of sensors to all blades is never desirable, and is certainly not practical outside of the design stage. This is due not only to the cost of instrumenting each blade, but also because of the complexities of bringing the measured signals to an external monitoring device. This needs to be done either with the use of slip rings or using a wireless telemetry system. Strain gauges are also located on the working engine surface areas such that they affect the aerofoil surface, and are exposed to the harsh internal engine environment, this not being conducive to sensor longevity.

Such are the difficulties of direct measurement of blade vibration, non-contact blade vibration measurement has been sought, with BTT methods showing the most promise and receiving research attention since the 1970's. Despite the promise of BTT methods they are still not without limitations or shortcomings four decades after their initial use. BTT is used in two different formats, being:

(i) Indirect methods where the blade displacement is measured while the engine speed is swept over a range such that a blade excitation frequency traverses a blade mode natural frequency. Estimates can then be made of the amplitude and natural frequency of the mode that is being excited. This was the original method of BTT, which used a single probe. A more recent advance in indirect measurement is the two parameter plot method developed by (Heath, 2000).

(ii) Direct BTT methods require constructing the sinusoidal forced displacement of a blade from the use of four or more probes. This method fits a sine wave to the measured data, with various methods of least square estimates of the fit used to minimise the effect of noise as is outlined by (Carrington et al., 2001). Also highlighted in (Carrington et al., 2001) was the effect that the spacing of the probe location, PSR, has on the sine wave it is able to estimate; for instance it was shown that if all probes were located within less than 30% of the wavelength of the fitted wave, poor data fits can be expected. To counteract the effect of the PSR, more than the minimum of four probes are used in more recent evolutions of this method. Some recent work which has shown the use of BTT methods to predict the displacement of blades, as compared to strain gauge measurements, is that of (Knappett and Garcia, 2008). This work showed that the estimated blade displacement from eight optical probes was in very good correlation with extrapolated strain gauge measurements applied to an FE model of the blades, for a single dominant excitation frequency, known in advance, and with well separated modes.

Another interesting recent alternative for non-contact measurement of blade vibrations is the use of a radar probe located in the casing periphery shown in the work of (Platt and Jagodnik, 2009). Good correlation was shown in the results when compared to strain gauge measurements on an experimental test engine. However, this technique, to date, is lacking in the presentation of sufficient technical detail to be able to follow up the results.

It was recently proposed by (Forbes and Randall, 2007) that blade vibration would have an effect on the casing wall pressure. Here, a simulated blade natural frequency was estimated by varying the rotation speed such that the blade excitation traversed the blade natural frequency and observing the increase in casing wall pressure frequency at harmonics of shaft speed. Unsteady casing wall pressure measurements have been used before this in an attempt to correlate blade condition with the pressure profile surrounding the blade, as in the following works (Mathioudakis et al., 1991, Dedoussis et al., 1994, Aretakis et al., 1998, Stamatis et al., 1997). This previous work had success in finding blade faults which affect the geometric periodicity of the blade passage pressure, such as a twisted blade. This causes changes in both the time passage of pressure past a certain measurement point and also

increases discrete harmonics of shaft speed in the pressure spectrum. Fault signatures were developed for a commercial gas turbine with seeded faults in (Mathioudakis et al., 1991). Some numerical analysis with increasing complexity was also shown to be able to deduce changes in the unsteady casing wall pressure and provide reliable fault signatures in (Dedoussis et al., 1994, Aretakis et al., 1998). Adaptive fluid dynamic modelling was eventually found to be able to predict the actual cascade geometric shapes from measured pressure signals producing reasonable estimates of blade altered geometry.

It is proposed in the work presented here that the pressure at the casing wall surface not only contains information about the static pressure profile around the blade, but the blade motion itself will alter the rotating pressure profile, such that the static pressure profile will follow the blade motion and will modulate the pressure profile of a blade. It is the phase demodulation of this pressure that will be able to give a measure of the blade motion amplitude at a given excitation frequency. Exploiting this change in casing wall pressure at harmonics of shaft speed, due to blade vibration, can then provide an alternative to BTT methods. It will be shown that this alternative has the potential to overcome the limitations on the number of sensors needed, and robustness to measurement noise. With some further work, it could be extended to the replacement of the pressure sensors with external casing accelerometers, then reducing any need for the sensor to be placed in the gas flow path.

BLADE PRESSURE PROFILE AND BLADE MOTION

If a blade is excited by one single dominant discrete frequency, then the motion of the blade tip for the 'rth' blade can be stated, without lose of generality, as:

$$x(t)_r = X_k \sin(k\Omega(t) + \gamma_k) \tag{1}$$

For the case of synchronous vibration in a gas turbine, 'k' is a positive integer and is often referred to as the engine order of excitation. If the blades have well separated modes and the excitation lies relatively close to one of the natural frequencies then X_k and γ_k can found from the solution of the forced vibration of the single degree of freedom system for the mode of interest.

With the assumption that the time averaged pressure profile around any blade is constant, the pressure profile around any blade can be described by a harmonic series, given by:

$$P_r = \mathrm{Re}\left\{\sum_{i=0}^{\infty} A_i P e^{ji[\theta+\Omega(t)+\alpha_r+\gamma_i]}\right\} \tag{2}$$

Where $j = \sqrt{-1}$ and A_i and γ_i are the amplitude and phase of the corresponding Fourier series. It is seen that equation (2) is a rotating wave form of any shape depending on the selected Fourier series co-efficients of A_i, γ_i and initial phase offset of α_r. For instance in Figure 1 a pressure profile shape is plotted, consisting of a raised cosine which spans one half blade spacing before and after each blade, for 6 rotor blades.

If we now make the assumption that the pressure profile around one blade follows the motion of that blade when it vibrates around its equilibrium position, then the pressure profile for the 'rth' blade will be modulated by the blade motion $x(t)_r$ such that the pressure profile can now be written as:

$$P_r = \mathrm{Re}\left\{\sum_{i=0}^{\infty} A_i P e^{ji[\theta+\Omega(t)+x(t)_r+\alpha_r+\gamma_i]}\right\} \tag{3}$$

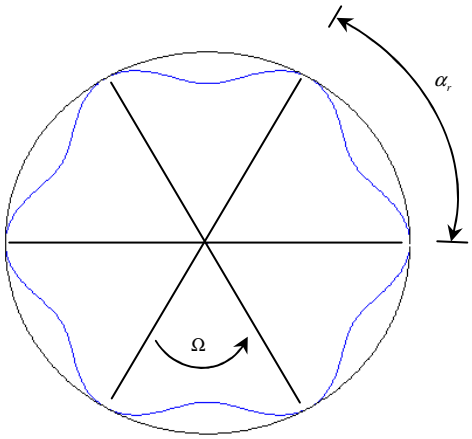

Figure 1 Schematic of simple first harmonic pressure distribution for a 6 bladed arrangement without blade motion

If we implement the Laurent power series expansion of an exponential function in terms of Bessel functions:

$$e^{x/2(t-1/t)} = \sum_{n=-\infty}^{\infty} J_n(x) t^n \tag{4}$$

then it can be seen that P_r is in the form of equation (4), such that P_r can now be written as:

$$P_r = \mathrm{Re}\left\{\sum_{i=0}^{\infty} A_i P e^{ji[\theta+\Omega(t)+\alpha_r+\gamma_i]} \sum_{n=-\infty}^{\infty} J_n(iX_k) e^{jn[k\Omega(t)+\gamma_k]}\right\} \tag{5}$$

Now taking the real part for all harmonics

$$P_r = \sum_{i=0}^{\infty}\sum_{n=-\infty}^{\infty} A_i P J_n(iX_k) \cos\begin{bmatrix} i(\theta+\Omega(t)+\alpha_r+\gamma_i) \\ +n(k\Omega(t)+\gamma_k) \end{bmatrix} \tag{6}$$

As the measured pressure at the casing wall, mathematically represented in equation (6), is a phase modulated signal, then phase demodulation would result in obtaining information about the modulating frequency i.e. $x(t)_r$ and the tip deflection X_k. However, a signal of the type as in equation (6) violates some assumptions for conventional demodulation techniques. For conventional phase demodulation the maximum modulation frequency must be at least less than half the carrier frequency to avoid aliasing. It can be seen that for the internal pressure signal this assumption will never be satisfied as multiple carrier frequencies exist at harmonics of shaft speed with the modulating frequency itself also a multiple of shaft speed. How to overcome the aliasing and demodulation of a signal of this type will be shown in the next section.

PRESSURE SIGNAL DEMODULATION

If we look at the special case of k = s, where s is the number of stator blades, and $\gamma_k = 0$, therefore:

$$k\Omega = s\Omega = \omega_{spf}$$

For illustration, if we also limit i < s then we can see the spectrum of the pressure signal will be a sum of discrete harmonics of 'i' with sets of sidebands at $\pm\ \omega_{spf}$. For instance the frequency at Ω will be made up of a component from Ω and $-(s-1)\Omega + \omega_{spf}$, see Figure 2.

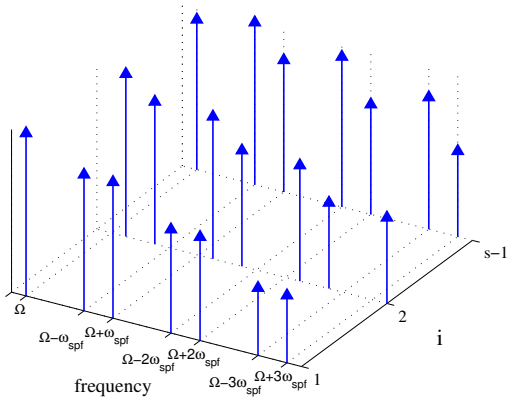

Figure 2 Discrete spectrum for carrier frequencies 'i' and modulating sidebands $\pm\ \omega_{spf}$.

Values of the measured pressure signal spectrum can be taken at frequency locations of $\Omega, \omega_{spf} - \Omega, \omega_{spf} + \Omega$, these being respectively y_1, y_{s-1}, y_{s+1}.

$$\begin{aligned} y_1 &= A_1 P J_0(X_s) + A_{(s-1)} P J_{-1}\left[(s-1)X_s\right] \\ y_{s-1} &= A_1 P J_{-1}(X_s) + A_{(s-1)} P J_0\left[(s-1)X_s\right] \\ y_{s+1} &= A_1 P J_1(X_s) + A_{(s-1)} P J_{-2}\left[(s-1)X_s\right] \end{aligned} \quad (7)\text{-}(9)$$

$A_1 P, A_{(s-1)} P, X_s$ are all unknowns. Now writing equations (7)-(9) in matrix form:

$$\mathbf{y} = \mathbf{D}\mathbf{x} \quad (10)$$

$$\mathbf{y} = \begin{bmatrix} y_1 & y_{s-1} & y_{s+1} \end{bmatrix}^T \qquad \mathbf{x} = \begin{bmatrix} A_1 P \\ A_{(s-1)} P \end{bmatrix} \quad (11)\text{-}(12)$$

$$\mathbf{D} = \begin{bmatrix} J_0(X_s) & J_{-1}\left[(s-1)X_s\right] \\ J_{-1}(X_s) & J_0\left[(s-1)X_s\right] \\ J_1(X_s) & J_{-2}\left[(s-1)X_s\right] \end{bmatrix} \quad (13)$$

Although (10) is not linear, it is linear for any value of X_s and can be solved by the linear least squares optimization of the over-determined system of equations (11)-(13). The estimate for the unknown co-efficients at any value of X_s is given by, in the least squares sense: (Handel, 2000)

$$\hat{\mathbf{x}} = \left(\mathbf{D}^T\mathbf{D}\right)^{-1}\mathbf{D}^T\mathbf{y} \quad (14)$$

To find the optimal value of X_s to fit the system of equations the non-linear least squares grid search is undertaken to maximise $g(x)$ (Handel, 2000), where

$$g(x) = \mathbf{y}^T\mathbf{D}\left(\mathbf{D}^T\mathbf{D}\right)^{-1}\mathbf{D}^T\mathbf{y} \quad (15)$$

A signal, of the type expressed in equation (6), that does not conform to the general requirements of conventional phase demodulation is therefore able to be demodulated with a non-linear least squares grid search fit of the spectrum.

General solution

For generality the phase offset angle, γ_k, of the driving frequency cannot be assumed to be zero, but will also be an unknown parameter; this causes the solution of the least squares non-linear grid search to be a function of two parameters, being X_k and γ_k.

In general, the co-efficients and angle of the spectrum at the 'tth' multiple of shaft speed can be shown to be:

$$\mathrm{Re}(y_t) = \sum_{z=0}^{z_{\max}} \left\{ \begin{matrix} A_e PCJ_h(eX_k)\cos\left[abs(h)\gamma_k\right] \\ -\phi A_e PSJ_h(eX_k)\sin\left[abs(h)\gamma_k\right] \end{matrix} \right\} \quad (16)$$

$$\mathrm{imag}(y_t) = \sum_{z=0}^{z_{\max}} \left\{ \begin{matrix} \phi d A_e PCJ_h(eX_k)\cos\left[abs(h)\gamma_k\right] \\ +d A_e PSJ_h(eX_k)\sin\left[abs(h)\gamma_k\right] \end{matrix} \right\} \quad (17)$$

where $z_{\max}$ is the number of columns in $\mathbf{D}$ and

$$C = \cos(e\alpha_r)$$
$$S = \sin(e\alpha_r)$$
$$\mathrm{mod}(t-z,k) = 0 \begin{cases} e = z-1 \\ h = (t-z)/k \end{cases}$$
$$\mathrm{mod}(t+z,k) = 0 \begin{cases} e = z-1 \\ h = -(t+z)/k \end{cases}$$
$$t = z \begin{cases} e = z-1 \\ h = 0 \end{cases}$$
$$else \begin{cases} e = 0 \\ h = 0 \end{cases}$$
$$\phi = \mathrm{sign}(h)$$
$$d = \mathrm{sign}(e + hk)$$

PRESSURE SIGNAL DEMODULATION WITH LIMITED FREQUENCY CONTENT

Observing equation (13) it can seen that in order to solve the least squares problem the number of columns in $\mathbf{D}$ must be greater than the number of rows, or in other words the amount of observable measurements in equation (11) must be large enough that the last observable measurement contains no information from the carrier frequencies. If we now introduce a small amount of white noise to the signal, SNR = 80, see Figure 3, then the sidebands begin to be buried in noise by the 20th shaft speed harmonic. In reality, the number of carrier harmonics may not only be significantly larger than the amount of shaft speed harmonics not affected by noise but their number is also unknown.

As the introduction of noise is unavoidable, some way of using only the initial shaft speed harmonics, which are much less noise affected, is needed. This can be done by exploiting the signal from another measurement location at a 90 degree offset from the first. Adding the initial signal with another signal at a 90 degree offset will then create a new pressure signal, $\hat{P}_r$, with every fourth shaft speed harmonic removed, starting at the second harmonic i.e. i = 2, 6,10 etc. see equation (20). This can be explained with a simplified example.

Creating a signal with the parameters given in Table 1, if we consider all harmonics of shaft speed up to the largest carrier frequency harmonic, in this case 24, then the size of $\mathbf{D}$ will have to have 24 columns and at least 25 rows, shown in equation (23). Reconstructed in equation (18) are the contributions to the casing wall pressure spectrum at the zero frequency.

Table 1 Parameter values for example 1, using a limited frequency range for demodulation.

X_s (rad)	s	b	max 'i' carrier harmonics	α_r (rad)	γ_k (rad)	Ω (Hz)
0.01	6	7	24	$\frac{\pi}{19}$	0	10

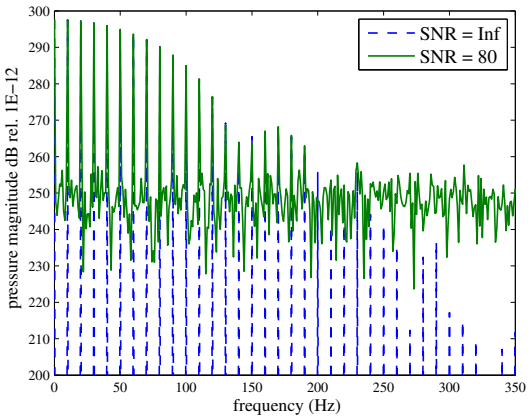

Figure 3 Spectrum of the casing wall pressure with values from Table 1.

$$y_o = J_o(0X_s)A_oP + J_{-1}(6X_s)A_6P + J_{-2}(12X_s)A_{12}P + J_{-3}(18X_s)A_{18}P... \quad (18)$$

For the above example

$$y_o = A_oP - 0.03A_6P + 0.0018A_{12}P - 0.00012A_{18}P... \quad (19)$$

It is evident that the influence of increasing carrier harmonics becomes increasingly insignificant, and the rate at which increasing carrier harmonics become insignificant is a function of the magnitude of X_s. If we truncate the series so that only the first 10 carrier frequencies are taken into account, this allows for at least the first two terms in the series to be present, and also taking measurements at the first 10 shaft speed harmonics, then we will now have a 10 x 10 square matrix, $\mathbf{D}$. For the system to be solved, as previously, then the system needs to be over-determined, so some columns need to be removed. It is seen that if we add a version of the signal measured at a 90 degree offset to the original this will remove the all the contributions at the 2, 6, 10, 14 etc shaft speed harmonics, therefore removing columns 2 and 6 in this example. This creates a new set of equations to be solved, $\hat{\mathbf{D}}$ and $\hat{\mathbf{x}}$, see equations (24) - (27), which are now over-determined and can be solved, as previously, in the least squares sense to estimate X_s from only the first 10 shaft speed harmonics. It should be noted that if the modulating frequency is a multiple of 4, then both the columns and rows that are multiples of 4 will be removed, such that the system of equations will not be over-determined and can not be solved in the least squares sense. If a probe was spaced at another location, say a 60 degree offset, then the same method could now be used for a modulating frequency with a multiple of 4, with deletion of every sixth row creating an over-determined system of equations again.

$$\hat{P}_r = \mathrm{Re}\left\{\begin{array}{l}\sum_{i=0}^{\infty} A_i P e^{ji[\Omega(t)+\alpha_r+\gamma_i]} \sum_{n=-\infty}^{\infty} J_n(iX_s) e^{jn(s\Omega(t)+\gamma_k)} \\ +\sum_{i=0}^{\infty} A_i P e^{ji[\pi/2+\Omega(t)+\alpha_r+\gamma_i]} \sum_{n=-\infty}^{\infty} J_n(iX_s) e^{jn(s\Omega(t)+\gamma_k)}\end{array}\right\} \quad (20)$$

$$\mathbf{y} = \begin{bmatrix}\mathrm{Re}(y_0)\\ \vdots \\ \mathrm{Re}(y_{25})\end{bmatrix} \qquad \mathbf{x} = \begin{bmatrix}A_oP\\ \vdots \\ A_{24}P\end{bmatrix} \quad (21)\text{-}(22)$$

$$\mathbf{D} = \begin{bmatrix} J_0(0X_s) & 0 & \cdots & 0 & J_{-4}(24X_s) \\ 0 & J_0(X_s) & \cdots & J_{-4}(23X_s) & 0 \\ \vdots & \vdots & \ddots & \vdots & \vdots \\ 0 & 0 & \cdots & 0 & J_0(24X_s)+J_{-8}(24X_s) \\ 0 & J_4(X_s) & \cdots & J_{-8}(23X_s) & 0 \end{bmatrix} \quad (23)$$

$$\mathbf{y} = \hat{\mathbf{D}}\hat{\mathbf{x}} \qquad \mathbf{y} = \begin{bmatrix}\mathrm{Re}(y_0)\\ \vdots \\ \mathrm{Re}(y_9)\end{bmatrix} \quad (24)\text{-}(25)$$

$$\hat{\mathbf{x}} = \begin{bmatrix}A_oP & A_1P & A_3P & A_4P & A_5P & A_7P & A_8P & A_9P\end{bmatrix}^T \quad (26)$$

$$\hat{\mathbf{D}} = \begin{bmatrix} J_0(0X_s) & 0 & 0 & 0 & 0 & 0 & 0 & 0 \\ 0 & J_0(X_s) & 0 & 0 & J_{-1}(5X_s) & J_{-1}(7X_s) & 0 & 0 \\ 0 & 0 & 0 & J_{-1}(4X_s) & 0 & 0 & J_{-1}(8X_s) & J_{-1}(9X_s)+J_{-2}(9X_s) \\ 0 & 0 & J_0(3X_s)+J_{-1}(3X_s) & 0 & 0 & 0 & 0 & 0 \\ 0 & 0 & 0 & J_0(4X_s) & 0 & 0 & J_{-2}(8X_s) & 0 \\ 0 & J_{-1}(X_s) & 0 & 0 & J_0(5X_s) & J_{-2}(7X_s) & 0 & 0 \\ 0 & 0 & 0 & 0 & 0 & 0 & 0 & 0 \\ 0 & J_1(X_s) & 0 & 0 & J_{-2}(5X_s) & J_0(7X_s) & 0 & 0 \\ 0 & 0 & 0 & J_{-2}(4X_s) & 0 & 0 & J_0(8X_s) & 0 \\ 0 & 0 & J_1(3X_s)+J_{-2}(3X_s) & 0 & 0 & 0 & 0 & J_0(9X_s)J_{-3}(9X_s) \end{bmatrix} \quad (27)$$

ADAPTIVE GRID REFINEMENT

For the above example the estimates of the blade tip deflection converge as shown in Table 2 and in Figure 4, it can be seen that convergence is reached when the grid had 1024 points, although at all times the answer was at the closest grid point to the solution. Obviously the accuracy, at best, is only ever going to be within half a grid spacing, therefore the spacing should be small around the solution to give better accuracy but does not need to be so fine away from the solution for efficiency. An adaptive grid scheme is therefore implemented, which splits the parameter space into a specified number of segments, where the number of solution points is one greater than the number of segments. The least squares gird search algorithm is then run so that a solution estimate is found. The parameter space is now split into the same number of segments, except that now the upper and lower bounds on the parameter space is given by the two grid points adjacent to the current solution. This is shown in the schematic in Figure 5, with a solution grid of five points across the parameter space of 0:0.2. The actual solution is shown by the square. The least squares solution for the given grid spacing is shown by the diamond for each grid refinement.

Table 2 Estimates of X_s for decreasing grid size. Grid is taken from 0:0.2, distance between grid points is 0.2/(grid spacing).

Normalised Grid size	Grid spacing	Estimate of X_s
1	2	0
2	4	0
3	8	0
4	16	0.0125
5	32	0.0125
6	64	0.0094
7	128	0.0094
8	256	0.0102
9	512	0.0102
10	1024	0.01

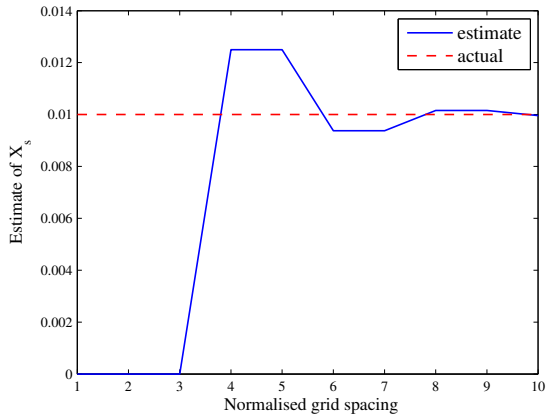

Figure 4 Convergence of X_s estimate for increasing normalised grid spacing

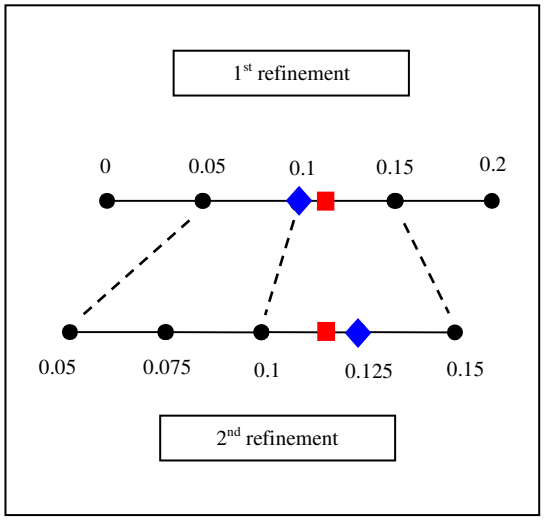

Figure 5 Schematic of adaptive grid refinement. Actual location of solution is shown by square ■, the solution grid is given by the black nodes. The least squares solution for the selected grid is given by the diamond. ◆

IMPLEMENTATION WITH MORE REALISTIC INPUT VALUES

If we now take a more realistic example using the values as given in Table 3 we can use the first 10 shaft speed harmonics to estimate the modulation frequency amplitude and phase. The grid refinement scheme is shown in Figure 6 for the first three grid refinements across the parameter space for

both X_s and γ_k. The grid can be seen to be refining around the solution, with both the estimated value and the real values given. In Figure 7 and Figure 8 the convergence of the estimates of X_s and γ_k is shown for more grid refinement iterations, in this case grid refinement is stopped after 8 iterations. It can be seen that the estimate for X_s converges on the actual value, as shown. However, the value for γ_k converges on an off-set value, and thus contains a bias. A bias is generally observed for all the estimates γ_k however the bias does not seem to have any significant impact on the estimate for X_s and as γ_k is not actually needed in these results, this bias does not seem to pose a problem.

Table 3 Parameter values for example with more realistic input values.

X_s (rad)	s	b	max 'i' carrier harmonics	α_r (rad)	γ_k (rad)	Ω (Hz)	SNR
0.01	6	19	48	$\frac{\pi}{19}$	$\frac{\pi}{7}$	10	∞

Some more simulations were run with additional values for SNR, see Figure 9 - Figure 11, for the parameters given in Table 3. Results are also shown for differing values of X_k and SNR, holding all the other parameters the same, as shown in each figure. The results show in general for SNR $\geq$ 3, X_k is estimated within a 15% error for values of X_k = 0.01. For greater values of X_k, the estimate can be given with a smaller error for more noisy data, see Figure 12. Conversely smaller values of X_k will be less predictable in less noisy data, Figure 13.

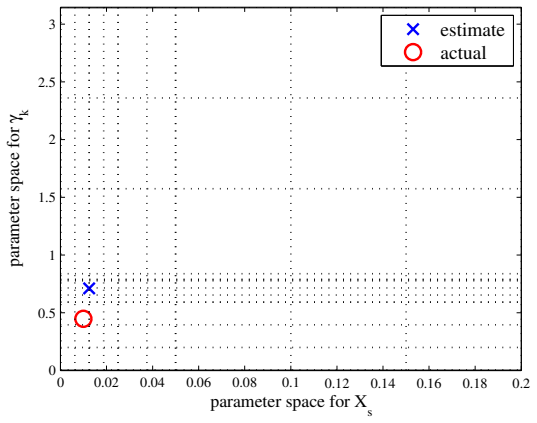

Figure 6 Estimates for X_s and γ_k for grid refinement up to 0.0031 and 0.0491 respectively.

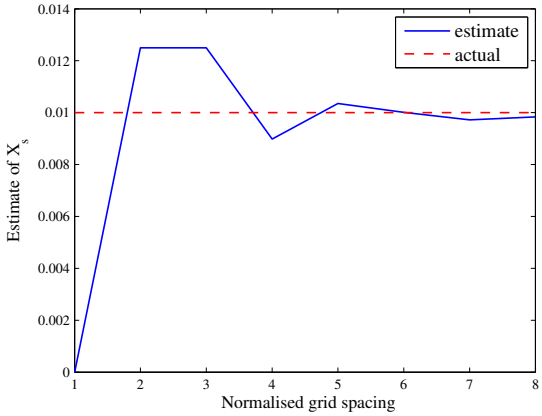

Figure 7 Convergence of X_s estimate for increasing normalised grid spacing with parameters from Table 3. Actual value of X_s as shown.

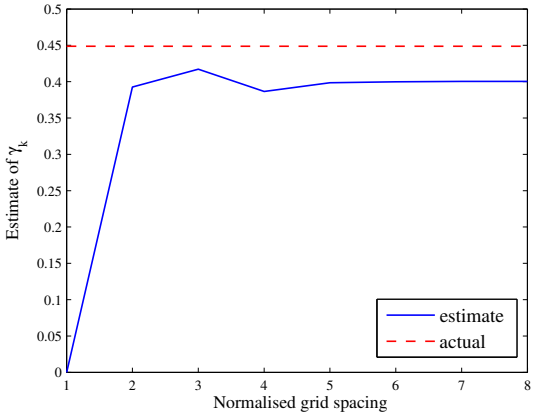

Figure 8 Convergence of γ_k estimate for increasing normalised grid spacing with parameters from Table 3. Actual value of γ_k as shown.

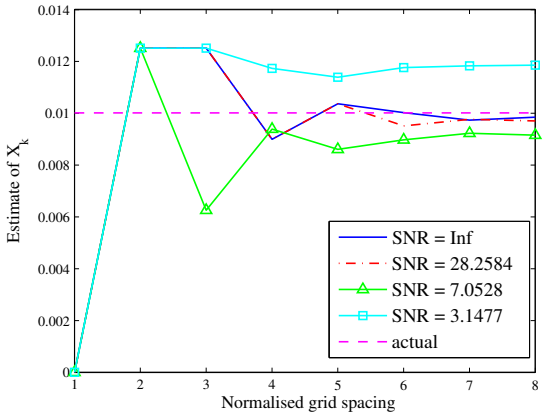

Figure 9 Convergence of X_k estimate for increasing normalised grid spacing with parameters from Table 3 with increasing SNR as shown. Actual value of X_k as shown.

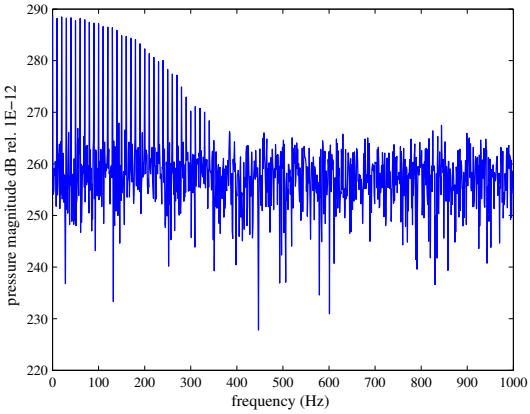

Figure 10 Spectrum of pressure signal with parameters from Table 3 and SNR = 3.1.

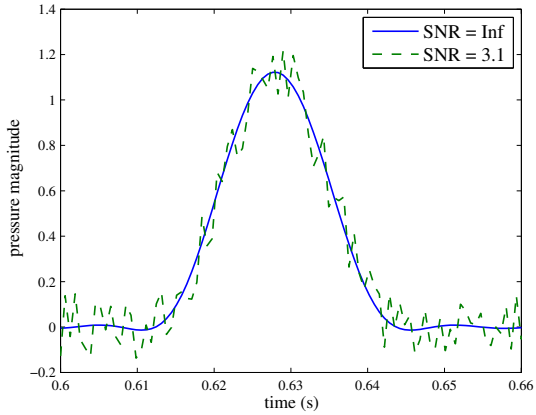

Figure 11 Time record of pressure signal with parameters from Table 3 shown is the noise free case and with a SNR = 3.1.

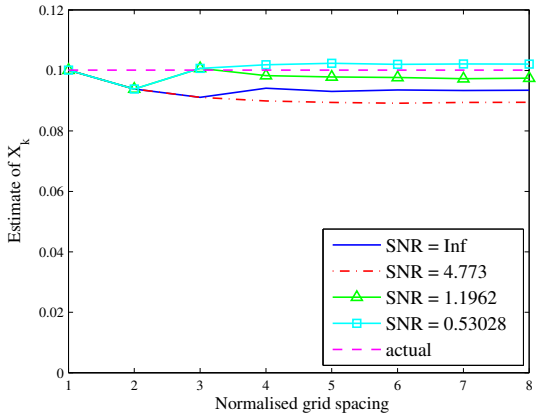

Figure 12 Convergence of X_k estimate for increasing normalised grid spacing with parameters from Table 3, with modified X_k as shown, and with increasing SNR as shown.

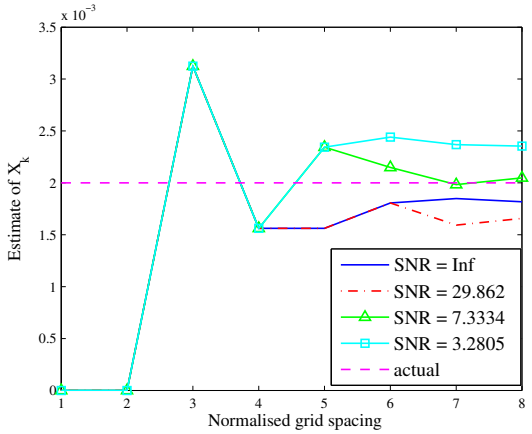

Figure 13 Convergence of X_k estimate for increasing normalised grid spacing with parameters from Table 3, with modified X_k as shown, and with increasing SNR as shown.

CONCLUSIONS

Simulated internal pressure signals from a gas turbine with the inclusion of blade vibration, has been presented along with a novel method of demodulating the casing wall pressure to estimate the blade vibration amplitude given a known single dominant driving frequency with well separated blade modes. The method has shown, with the simulated values, a robustness to noise for small blade deflection values.

Some of the limitations currently on BTT methods have been shown to be removed with measurement of the casing wall pressure. Only a limited number of sensors is needed, and there is no limit on the probe spacing ratio. Some further research enabling the pressure measurements to be replaced with the measurement of casing vibrations would also allow the sensors to be located outside of the gas path, providing significant advantage.

ACKNOWLEDGEMENTS

Grateful acknowledgment is made for the financial assistance given by the Australian Defence Science and Technology Organisation, through the Centre of Expertise in Helicopter Structures and Diagnostics at UNSW.

REFERENCES

Aretakis, N., Mathioudakis, K. & Dedoussis, V. (1998) *Derivation of signatures for faults in gas turbine compressor blading*. Control Engineering Practice, 6**,** 969-974.

Carrington, I. B., Wright, J. R., Cooper, J. E. & Dimitriadis, G. (2001) *A comparison of blade tip timing data analysis methods*. Proceedings of the Institution of Mechanical Engineers, Part G: Journal of Aerospace Engineering, 215**,** 301-312.

Dedoussis, V., Mathioudakis, K. & Papiliou, K. D. (1994) Numerical simulation of blade fault signatures from unsteady wall pressure signals. Hague, Neth, Publ by ASME, New York, NY, USA.

Forbes, G. L. & Randall, R. B. (2007) Simulated Gas Turbine Casing Response to Rotor Blade Pressure Excitation. *5th Australasian Congress on Applied Mechanics.* Brisbane, Australia.

Handel, P. (2000) *Properties of the IEEE-STD-1057 four-parameter sine wave fit algorithm*. IEEE Transactions on Instrumentation and Measurement, 49**,** 1189-93.

Heath, S. (2000) *A New Technique for Identifying Synchronous Resonances Using Tip-Timing*. Journal of Engineering for Gas Turbines and Power, 122**,** 219-225.

Knappett, D. & Garcia, J. (2008) *Blade tip timing and strain gauge correlation on compressor blades*. Proceedings of the Institution of Mechanical Engineers, Part G (Journal of Aerospace Engineering), 222**,** 497-506.

Mathioudakis, K., Papathanasiou, A., Loukis, E. & Papailiou, K. (1991) *Fast response wall pressure measurement as a means of gas turbine blade fault identification*. Journal of Engineering for Gas Turbines and Power, Transactions of the ASME, 113**,** 269-275.

Platt, M. J. & Jagodnik, J. J. (2009) Non-contacting measurement of turbomachinery blade vibration. *MFPT 2009.* Dayton, Ohio, USA.

Stamatis, A., Aretakis, N. & Mathioudakis, K. (1997) Blade fault recognition based on signal processing and adaptive fluid dynamic modelling. Orlando, FL, USA, ASME, New York, NY, USA.